ADVANCED ELECTRONIC MATERIALS Open Access
www.advelectronicmat.de

Transfer of Millimeter-Scale Strained Multiferroic Epitaxial Thin Films on Rigid Substrates via an Epoxy Method Producing Magnetic Property Enhancement

James P. Barnard, Yizhi Zhang, Lizabeth Quigley, Jianan Shen, Benson Kunhung Tsai, Max R. Chhabra, Jiho Noh, Hyunseung Jung, Oleg Mitrofanov, Raktim Sarma, Aleem Siddiqui, Igal Brener, Chloe F. Doiron, and Haiyan Wang**

The demonstration of epitaxial thin film transfer has enormous potential for thin film devices free from the traditional substrate epitaxy limitations. However, large-area continuous film transfer remains a challenge for the commonly reported polymer-based transfer methods due to bending and cracking during transfer, especially for highly strained epitaxial thin films. In this work, a new epoxy-based, rigid transfer method is used to transfer films from an $SrTiO_3$ (STO) growth substrate onto various new substrates, including those that will typically pose significant problems for epitaxy. An epitaxial multiferroic $Bi_3Fe_2Mn_2O_x$ (BFMO) layered supercell (LSC) material is selected as the thin film for this demonstration. The results of surface and structure studies show an order of magnitude increase in the continuous area of transferred films when compared to previous transfer methods. The magnetic properties of the BFMO LSC films are shown to be enhanced by the release of strain in this method, and ferromagnetic resonance is found with an exceptionally low Gilbert damping coefficient. The large-area transfer of this highly strained complex oxide BFMO thin film presents enormous potential for the integration of many other multifunctional oxides onto new substrates for future magnetic sensors and memory devices.

1. Introduction

Multiferroic thin film oxides possessing two or more ferroic orders,[1,2] e.g., ferromagnetism and ferroelectricity, are a promising platform for innovative memory devices,[3–7] computing paradigms,[8] acoustic sensors,[9–12] and integrated photonics.[13–15] Achieving single-phase multiferroic thin films is challenging because the electronic requirements are seemingly at odds, typically requiring both unpaired electron spins, for ferromagnetism, and empty d-orbitals, for ferroelectricity.[2] Among all single-phase multiferroic materials, the $Bi_3Fe_2Mn_2O_x$ (BFMO) layered supercell (LSC) is a promising material with this rare combination and is therefore an ideal platform for addressing challenges requiring multiferroics.[16–24] Current methods of depositing BFMO require the use of strained epitaxial growth on a conventional lattice-matched substrate—generally $SrTiO_3$ (STO) or $LaAlO_3$ (LAO).[25] While these films exhibit excellent magnetic and ferroelectric[18,21–24,26,27] properties, the use of STO and LAO substrates precludes these films from being integrated with next generation four-state memory,[3,6] THz emitters,[28,29] and magnetic tunnel junctions,[3] which require the use of fused silica,[13,15] lithium niobate,[9–12] silicon,[30–32] and sapphire[33,34] substrates.

J. P. Barnard, Y. Zhang, L. Quigley, J. Shen, B. K. Tsai, M. R. Chhabra, H. Wang
School of Materials Engineering
Purdue University
West Lafayette, IN 47907, USA
E-mail: hwang00@purdue.edu

The ORCID identification number(s) for the author(s) of this article can be found under https://doi.org/10.1002/aelm.202400492

DOI: 10.1002/aelm.202400492

J. Noh, H. Jung, O. Mitrofanov, R. Sarma, A. Siddiqui, I. Brener, C. F. Doiron
Sandia National Laboratories
Albuquerque, NM 87185, USA
E-mail: cfdoiro@sandia.gov

J. Noh, H. Jung, O. Mitrofanov, R. Sarma, I. Brener, C. F. Doiron
Center for Integrated Nanotechnologies
Sandia National Laboratories
Albuquerque, NM 87185, USA

O. Mitrofanov
Electronic and Electrical Engineering
University College London
London WC1E 7JE, UK

H. Wang
School of Electrical and Computer Engineering
Purdue University
West Lafayette, IN 47907, USA

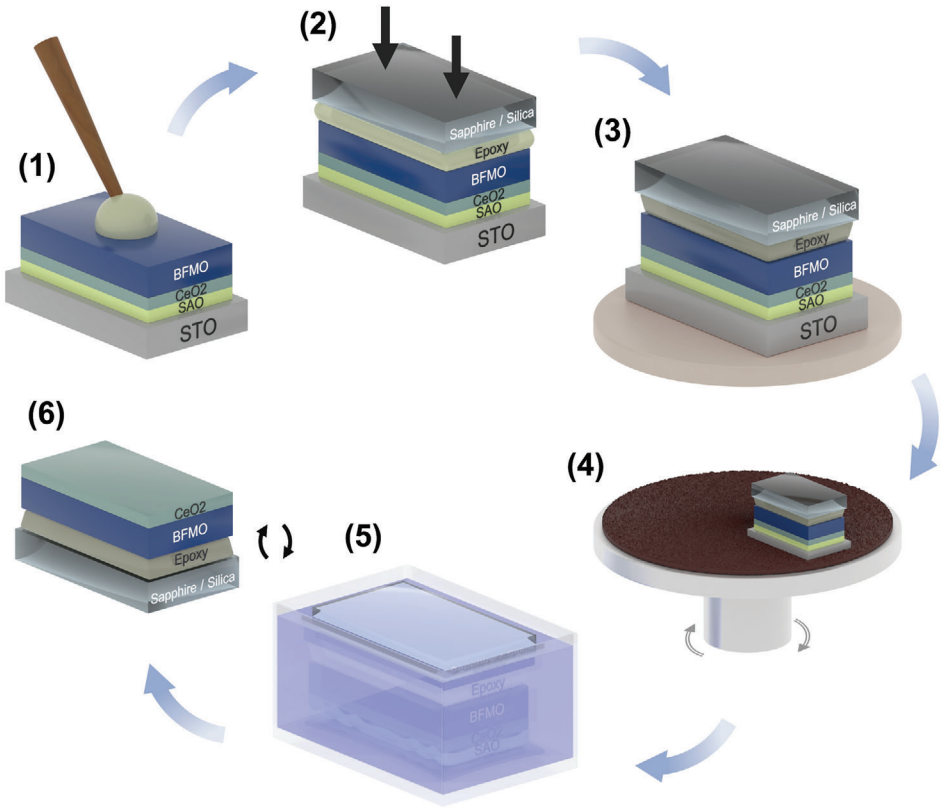

Figure 1. Schematic overview of transfer process of BFMO thin film by SAO water-soluble layer and rigid substrate epoxy method. The steps are 1) epoxy application, 2) initial bonding, 3) curing, 4) lapping, 5) release layer dissolution, and 6) final cleaning.

While buffer layers allow growth of such oxide thin films on epitaxially mismatched substrates, these growth methods require time-intensive optimization that is unique to a specific film-substrate combination.[17,23,32,35,36] Moreover, the use of buffer layers for amorphous substrates—where no crystal structure is available to seed the film—or polycrystalline substrates—with random grain orientations—presents an even larger challenge necessitating the development of more complex growth processes. One method of overcoming film-substrate epitaxial mismatch is thin film transfer through the introduction of release layers,[37–44] which allow the deposited film to be peeled away from the substrate, with two predominant release strategies: 1) 2D van der Waals (vdW) materials, such as graphene or transition metal dichalcogenides (TMDs),[38,40,42,45] and 2) dissolvable epitaxial layers, such as $La_{0.6}Sr_{0.3}MnO_3$ (LSMO) or $Sr_3Al_2O_6$ (SAO).[41,46–51] While the insertion of vdW materials enables direct epitaxial growth and easy removal of the film for transfer, it is unknown whether remote epitaxy—a necessity for this type of growth—would work with highly strained systems.[52] In comparison, the use of dissolvable epitaxial layers allows not only easy film removal without damaging the film (using HCl for LSMO and H_2O for SAO), but also provides a straightforward path for growing even highly strained films.

While sacrificial epitaxial layers allow for easy removal, existing methods for film transfer are unsuitable for highly strained materials. Commonly, for unstrained epitaxial materials, a flexible polymer substrate such as polypropylene carbonate (PPC) or poly(dimethylsiloxane) (PDMS) can be attached to the film before dissolving the sacrificial layer, providing structural support while placing the film onto the new substrate.[37–42] After adhering the film to the new substrate via pressure and temperature, the polymer layers are peeled off, dissolved, or evaporated, leaving the single-crystal film bonded to the new substrate. While this approach works well for unstrained materials, when transferring highly strained epitaxial films, such as BFMO, the substrate clamping effect is lost upon release from the growth substrate, relaxing the built-in strain and leading the film to wrinkle or curl, resulting in the formation of cracks and fragmented regions.[51] These defects drastically reduce the continuous area of transferred films with current demonstrations failing to reach the millimeter scale.[53] The lack of large area transfer methods prevents the use of BFMO for applications such as surface acoustic wave devices,[10] acoustically driven ferromagnetic resonance (ADFMR) transducers,[9,11,12,54] and topological insulators.[55,56]

In this work, we demonstrate large-area film transfer using a new rigid substrate transfer method that relies on thermoset epoxy. This method entails adhering the film to a rigid destination substrate—sapphire or fused silica in this work—using a thin layer (<1 μm) of epoxy, as illustrated in **Figure 1**. This creates a "sandwich" with the film between the original substrate and new substrate. The film is then left attached to the new substrate after the SAO sacrificial layer is dissolved. Since the film is not freestanding or allowed to bend at any time during the process, we believe that the strain should not be fully relaxed. This

is desirable as relaxation would lead to surface deformation. This demonstration uses multiferroic BFMO films deposited on STO substrates. Our results exhibit large, crack-free areas of transferred BFMO film. We characterize and compare the microstructure and magnetic properties of the film before and after transfer. When compared to flexible polymer methods, the transferred areas are improved from hundreds of microns to several millimeters, a phenomenal result for device fabrication. Finaly, we conduct ferromagnetic resonance (FMR) measurements to explore the spin dynamics in the BFMO thin films, discovering that this material has excellent damping properties with a low Gilbert damping coefficient.

The transfer process demonstrated in this work can be broken into six steps, as shown schematically in Figure 1. Additional details about the transfer process can be found in the Methods section. 1) A sacrificial layer of water-soluble SAO is deposited directly on top of the STO substrate, followed by the CeO_2 buffer layer and the main BFMO film. After deposition, a small drop of epoxy is applied to the surface of the film. 2) The new substrate is placed on top of the epoxy and pressed down to form a thin epoxy layer. 3) The sample is heated on a hot plate to cure the epoxy. 4) A large portion of the STO thickness is removed by lapping. 5) The sample is placed in water, allowing the SAO layer to dissolve. The STO pulls away from the film as the SAO dissolves, leaving only the film, epoxy, and new substrate. 6) The sample is removed from the water and cleaned to remove SAO residue. The final result is the BFMO film bonded to the new substrate by epoxy.

2. Results

It is important to observe the film quality during transfer as the SAO dissolution process is known to introduce cracks in several ways.[57–60] First, the strong physical bonds present in oxides only allow for minimal compliance, quickly leading to cracks when the film is released. Second, defects generated by misfit strain relaxation can be the source of cracks during transfer. To characterize this, various surface measurements were performed. Optical microscopy was used throughout the transfer process to analyze the surface of the film and optimize each transfer step. The images shown in **Figure 2**a,e are taken after film deposition and before applying the epoxy, for the samples transferred onto sapphire and fused silica, respectively. The surface has minimal interference fringes due to slight thickness variations in the film, deposited by PLD. While these thickness variations are not desirable, this is a common shortcoming of PLD due to the typical plasma plume shape. No thickness effects were observed throughout the transfer process. Figure 2b,f shows the surface, as viewed through the new transparent substrate, after applying and curing the epoxy. After lapping the STO to a thickness of 30 µm, Figure 2c,g is collected, showing very minimal damage to the film around the edges of the substrate area. The center of the film appears to be free of damage. Figure 2d,h shows the final surface of the film after dissolving the SAO sacrificial layer and completely removing the original STO substrate. The heating and sonication required to fully dissolve the SAO layer, discussed more in the Methods section, result in some additional damage to the film, but large areas (≈3 × 3 mm) of film still appear to be damage free on both the sapphire and fused silica substrates. The difference between these two transferred samples can be attributed to differences in the epoxy adhesion on each substrate.

Atomic force microscopy (AFM) was used to analyze the post-transfer surface morphology. As shown in Figure 1 step 6, the thin CeO_2 film is now on top of the primary BFMO film. Therefore, the surface roughness is dictated by the original interface between the SAO layer and the CeO_2 layer. This gives the added benefit of low surface roughness, as seen in Figure 2i,j for the sapphire and fused silica samples, respectively. The terrace-like structure visible in these scans has been previously reported in CeO_2.[61,62] The peak-to-peak surface roughness is ≈8 nm in both samples. The surfaces were also analyzed using scanning electron microscopy (SEM) to determine the presence of microscopic cracks or fragmentation in the film, which was one of the significant issues with previous transfer methods, as discussed previously. Figure 2k,l shows the high magnification images for the sapphire and fused silica substrates, respectively. No cracks or other damage to the film is observed in this area of the film. Low mag SEM images are included in Figure S1 (Supporting Information), showing that no damage is visible across the larger area either. Some small particles are visible in the AFM and SEM scans due to sample handling. These results are excellent and indicate that the goal of achieving mm-scale continuous transferred films has been reached.

After analyzing the surface film quality, it is also important to confirm that the structure and crystallinity of the films have been maintained, as these parameters can have a significant impact on the properties of the film. To study this, x-ray diffractometry (XRD) was used. A 2θ-ω scan, shown in **Figure 3**a, indicated a high crystalline quality of the films as-deposited on the STO substrate, with the peaks corresponding to the BFMO LSC phase indicated with "SC" in the plot. The sharp (001) family peaks provide evidence of the crystalline nature and monoaxial alignment of the BFMO, CeO_2, and SAO films. The full-width at half-maximum (FWHM) values of the BFMO peaks are comparable to those reported in previous works with epitaxial BFMO.[17,19–21,24] Since the grain boundaries present in films with random in-plane orientations are expected to increase the FWHM of the peaks, this data indicates that the films may be biaxially epitaxial. After transferring the film onto fused silica and sapphire, the 2θ-ω scans were repeated and are shown in Figure 3b,c. The film maintains its strong crystalline structure and monoaxial alignment as demonstrated by the sharp (001) family peaks. The SAO peaks are still visible due to residue left after the dissolution process and the fact that a minor phase in BFMO overlaps with this peak.[22] The peaks marked with "*" correspond to an alternate BFMO phase with a different Bi stoichiometry. This phase is not the primary phase, shown by the much lower intensity of these peaks, and it is expected to have minimal contributions to the properties. To further analyze the structure, rocking curves were collected for all three samples. The as-deposited sample is shown in Figure 3d with a full-width and half-max (FWHM) of 0.339°. In comparison, the transferred films are shown in Figure 3e,f with FWHM values of 0.562° and 0.546° on fused silica and sapphire, respectively. The slightly higher FWHM values indicate the generation of low-angle grain boundaries, cracks, or other defects during the transfer process. These defects are found in the visibly damaged parts of the film and are caused by poor adhesion to the new substrate in those areas. However, this data still shows high-quality

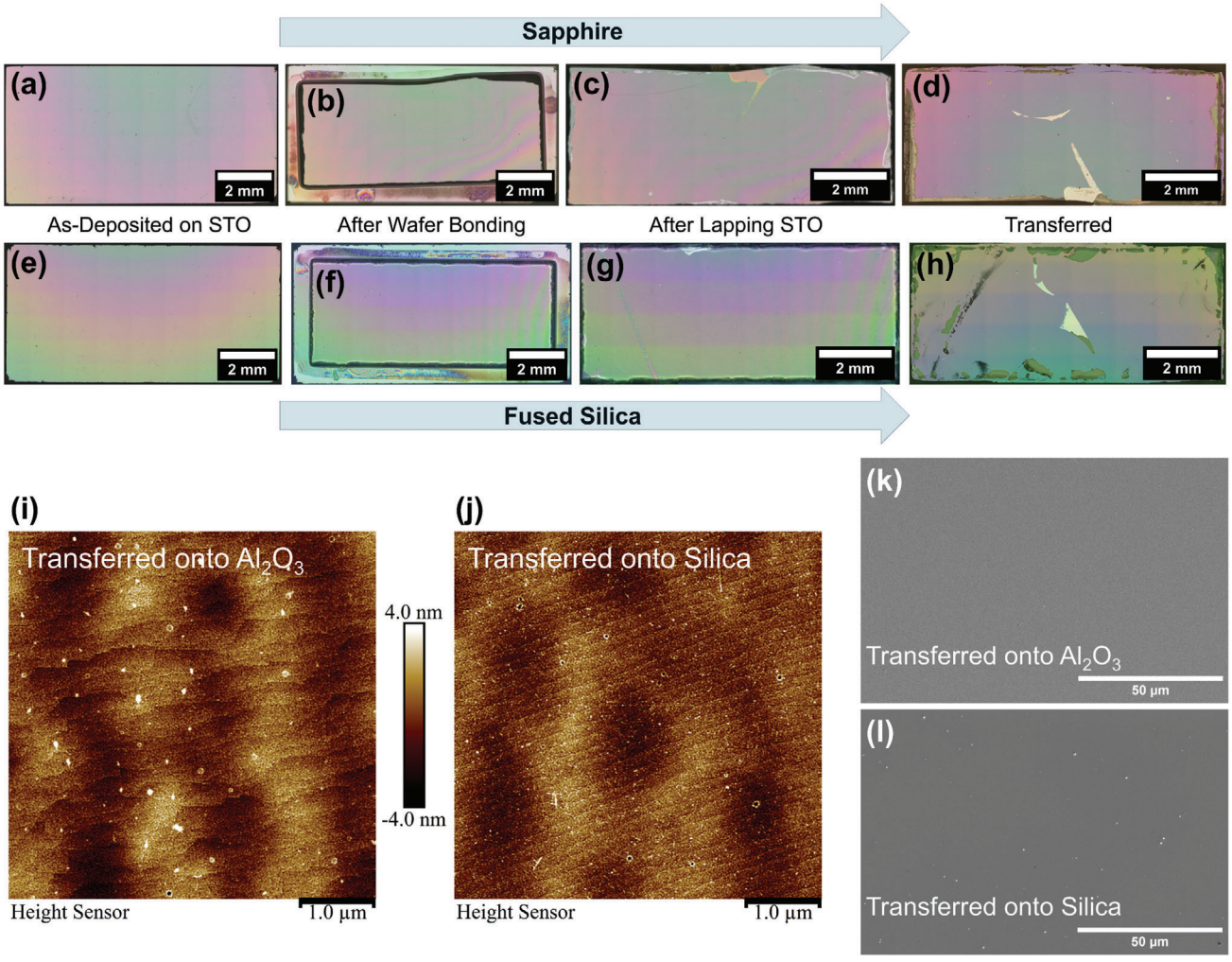

Figure 2. Transfer quality analysis before and after transfer. Optical images of sample surface throughout the transfer process for films transferred onto new a–d) sapphire and e–h) fused silica substrates. Surface roughness of the final transferred film on i) sapphire and j) fused silica. SEM images showing crack-free areas of transferred films on k) sapphire and l) fused silica.

films after transfer with no damage in the large continuous areas of the film, in agreement with what is seen in other works on unstrained films.[39,41]

To further analyze the structure and epitaxial state of the BFMO film, transmission electron microscopy (TEM) analysis was conducted on the cross-section samples before and after transfer. As a starting point, a CeO_2/BFMO film was deposited directly on STO for imaging. This reference sample was grown without the SAO sacrificial layer to allow a full analysis of the effects of the transfer process and the introduction of the required SAO layer. As previously mentioned, CeO_2 is commonly used as a buffer layer for BFMO as it promotes the epitaxial growth of the LSC phase. This is due to the zigzag bonding structure of CeO_2, which matches that of the BFMO LSC.[17] The zigzag structure of the CeO_2, marked with green circles, can be seen in the scanning TEM (STEM) image in **Figure** 4a. STEM images show *Z*-contrast for composition related study (contrast $\approx Z^{1.7}$).[63] The clear layered structure of the BFMO LSC can also be observed and is imaged in at a higher quality in Figure 4b. As indicated by the blue and white circles, the cations present in BFMO self-assemble into alternating bilayers of Bi_2O_2 and MnO_6/FeO_6.[21] The self-assembly of this layered structure in a one-step deposition in observed in all Aurivillius phases.[26] The BFMO films imaged here have clear biaxial alignment and epitaxy with the STO substrates, observed by the alignment of the crystal planes in both directions. This epitaxial relationship agrees with previous reports of the BFMO LSC structure grown on STO both with and without the CeO_2 buffer layer.[16–21,24]

After completing the transfer of the CeO_2/BFMO film, a cross-section TEM sample was prepared by focused ion beam (FIB) for the transferred sample on sapphire, as shown in Figure 4c,d. The sapphire sample was selected to investigate whether the crystallinity of the new substrate had any impact on the transferred film. The first image shows a STEM capture of the entire layer stack. The BFMO and CeO_2 layers are now reversed due to the nature of the transfer process. The organic epoxy material can be seen directly contacting the BFMO film. The Pt layers at the top of the image are conductive and protective layers used in the TEM

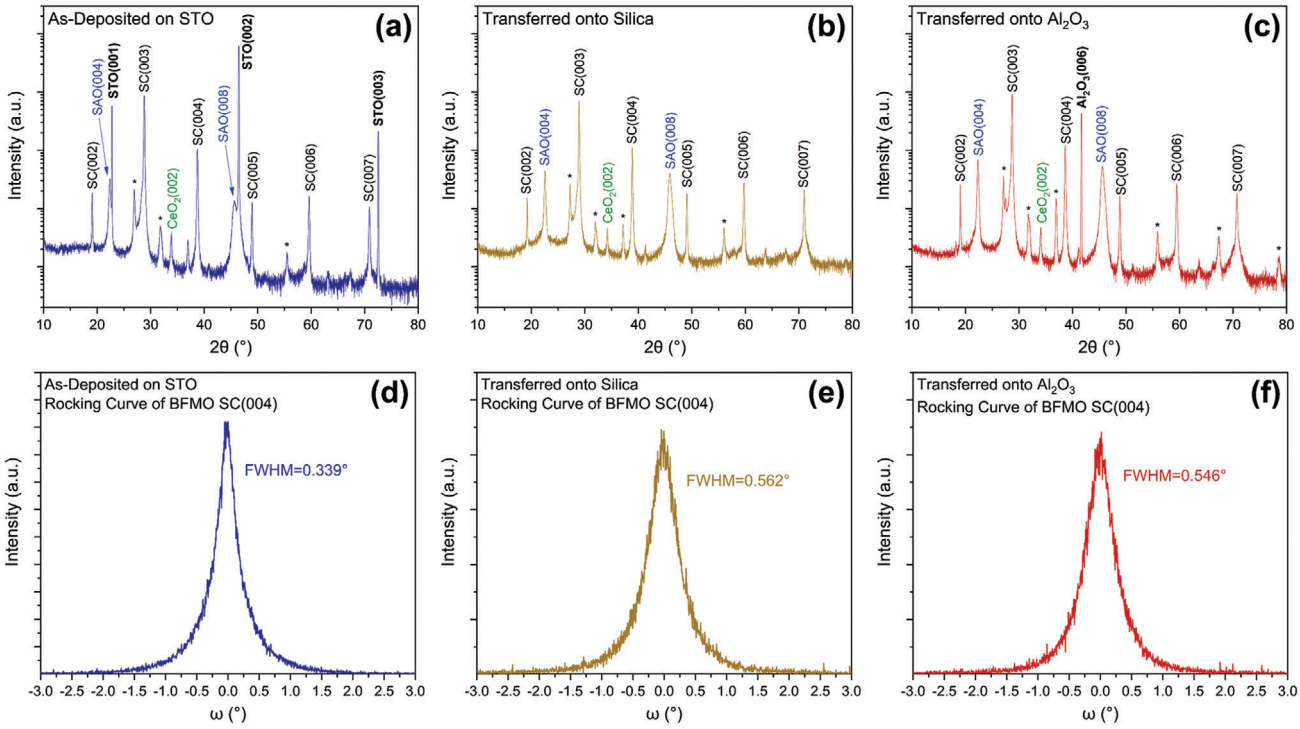

Figure 3. Film structure analysis before and after transfer. XRD a–c) 2θ-ω scans and d–f) rocking curves for BFMO films a,d) as-deposited on STO, b,e) transferred onto fused silica, and c,f) transferred onto sapphire. The peak label "SC" corresponds to the layered supercell phase of BFMO. The peaks indicated with a "*" correspond to a minor, alternate BFMO phase.

lift-off process. Figure 4d shows elemental mapping of the sample by energy-dispersive x-ray spectroscopy (EDS). The Ce and Bi, shown in blue and red, respectively, indicate the location of the CeO_2 and BFMO layers. While the microstructure of the layers cannot be seen in these images due to the relatively thick TEM foil by FIB, they still confirm that the layers are free from significant damage. The XRD data from Figure 3 confirms the high crystallinity of the transferred sample. A low-magnification image of the entire sample thickness is shown in Figure S2 (Supporting Information), where the sapphire substrate is also visible. Figure S3 (Supporting Information) includes the EDS images of the remaining relevant elements in the film for the same field of view as the images shown in Figure 4c,d.

To further confirm that the transfer process did not cause damage to the film, the physical properties of the BFMO LSC were also studied. Specifically, a focus was placed on the magnetic properties considering its potential for FMR applications. The as-deposited sample (with the SAO sacrificial layer) was first measured and is shown in **Figure 5**a,b for room temperature and low temperature, respectively. At room temperature, the magnetic saturation and coercivity are relatively low, 1.5–2.5 emu cm^{-3} and 100 Oe, respectively; comparable with that reported in other works for the BFMO LSC and BFMO pseudocubic structures.[22,23,64] At low temperature, the magnetic saturation increases to 30 emu cm^{-3}. Since there are no magnetic transitions between 300 and 10 K, the increase in attributed to decreased thermal action at low temperature.[23]

Surprisingly, when the magnetic properties are measured after transfer, the results are not what was initially expected. The sample selected for post-transfer magnetic measurements was on the sapphire substrate since this film had a larger continuous area, which is important for accurate magnetic measurements. Figure 5c,d shows these measurements for the transferred sample at room temperature and low temperature, respectively. While the film structure has been shown to be nearly the same before and after transfer, the magnetic saturation is significantly higher than that in the as-deposited sample at 26 emu cm^{-3} at room temperature and 74 emu cm^{-3} at low temperature. Additionally, the coercivity was found to increase, particularly in the low temperature measurement, where the value changed from 800 Oe before transfer to 1400 Oe after transfer. We attribute the increase magnetic saturation and coercivity to a partial relaxation of strain in the film. The as-deposited BFMO film has a high misfit strain, as reported in previous works, and the post-transfer sample may be losing strain to relaxation during transfer.[16–19,22,24] Going back to the XRD data in Figure 3a,c, a comparison of the highest intensity BFMO SC(003) peak position for the as-deposited and transferred films shows a change of 0.1° in 2θ. This change confirms that a partial strain relaxation took place during the transfer process. The magnetic properties of the BFMO LSC are known to fluctuate based on the strain state of the film due to the magnetoelastic coupling effect.[20] In $BiFeO_3$ (BFO) thin films, which are similar in composition to BFMO, the magnetic properties have also been found to change when the strain was altered through substrate selection.[65] During the transfer process, the film is released from the growth substrate and the strain can partially relax, although the epoxy still locks the film in place on the top surface. Increased magnetic saturation has been previously reported

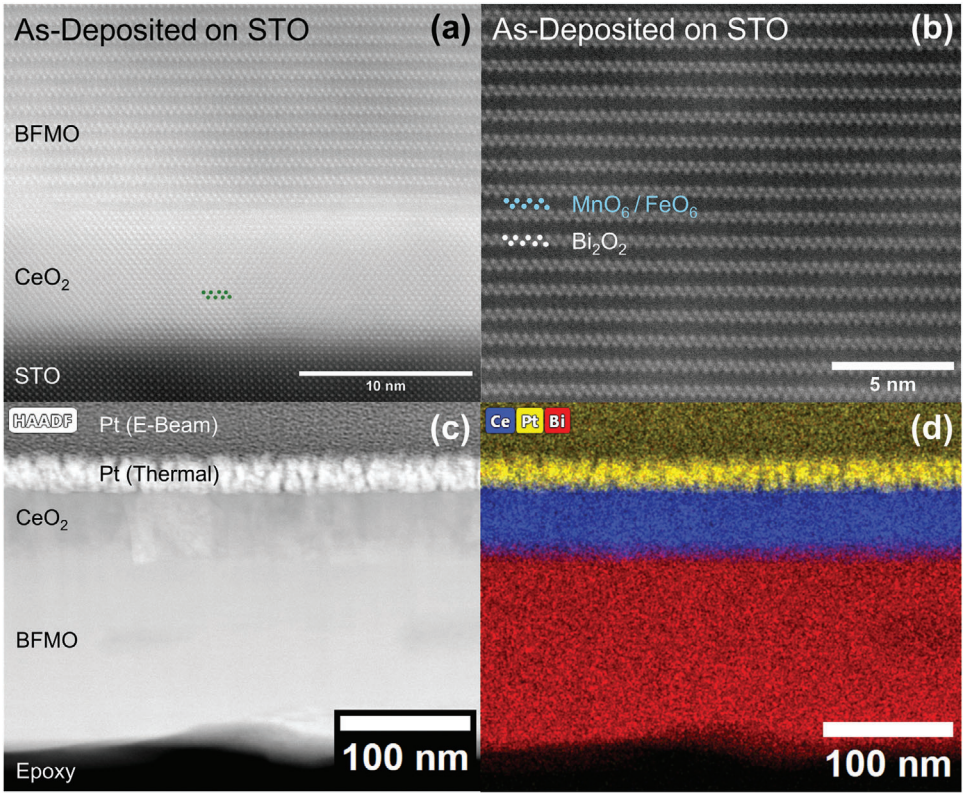

Figure 4. TEM analysis of film structure and composition. a,b) STEM images of CeO_2/BFMO film deposited directly on an STO substrates. The two magnification levels show the full layer stack and the atomic structure of the BFMO LSC. c) STEM image of film transferred onto sapphire showing the film stack and the epoxy. d) Elemental mapping EDS image of the same area showing the locations of each film.

in various thin film materials when releasing the strain in magnetic thin films either by transfer or by substrate selection.[41,66] In the case of transferred BFMO, we theorize that the increased magnetic saturation may be due to the change in interatomic spacing as the strain is changed which causes the spins to interact differently. A complete understanding of this mechanism requires a controllable range of strain states, such as by selecting a larger range of substrates or through a sample bending study, which could be the topic of another work.

It is important to note that the new materials added to the sample during transfer are not expected to impact the measurement. Both the new sapphire substrate and organic epoxy material are diamagnetic and are therefore isolated from the measurement during the background signal removal.[67,68]

Based on the strong magnetic properties of this BFMO material, the FMR properties were explored. In previous reports, the FMR characteristics have only been measured in the pseudocubic phase of BFMO, which is known to have different functional properties than the LSC phase.[22,69] FMR data was collected on the as-deposited on STO sample. In this measurement, the microwave frequency was fixed for each measurement (9–17.5 GHz) and the DC applied magnetic field was swept across the range where the resonance peak is expected to be located. The FMR signal for each of these scans is shown in **Figure 6a**. The peaks are not all perfectly symmetric due to the Fano-type resonance.[70] Interestingly, most of the frequencies probed exhibit three discrete peaks, rather than a single peak. A zoomed view of a single frequency is shown in Figure S4 (Supporting Information) to better display the triple peak nature. While the center peak has the highest intensity and was used for the following calculations, the side peaks still rise significantly above the noise floor. The generation of multiple peaks is believed to be due to the unique periodic layered structure of the BFMO LSC, which is spatially non-uniform. The discrete layers of Bi_2O_2 and MnO_6/FeO_6 may present slightly different resonances. In addition, the Mn and Fe-rich areas visible in the elemental maps in Figure S3 (Supporting Information) may give rise to the secondary resonance peaks. Another possible cause of the satellite peaks is standing spin waves along the lateral direction of the film. The field-swept linewidth of each peak was measured and compiled into a plot versus the microwave frequency, as shown in the Kittel plot in Figure 6b. By applying a linear fit, the ΔH_0 value was found to be 15.567 Oe. These resonance peaks have a notably high Q-factor. The resonance field at each frequency was also plotted, shown in the damping plot in Figure 6c. By once again fitting a line to the data, the Gilbert damping coefficient (α) was found to be 0.00025 or 2.5×10^{-4}, a notably lower coefficient than the value of 0.0034 reported in the previous BFMO work.[69] The Gyromagnetic Ratio ($\gamma/2\pi$) was calculated as 28.081 GHz/T. Interestingly, initial FMR measurements on the post-transfer samples did not show the resonance peaks that are seen in the as-deposited sample. These results suggest that additional optimization efforts on the FMR measurements are needed to locate the resonance peaks in the transferred samples. In addition, there may be microscopic

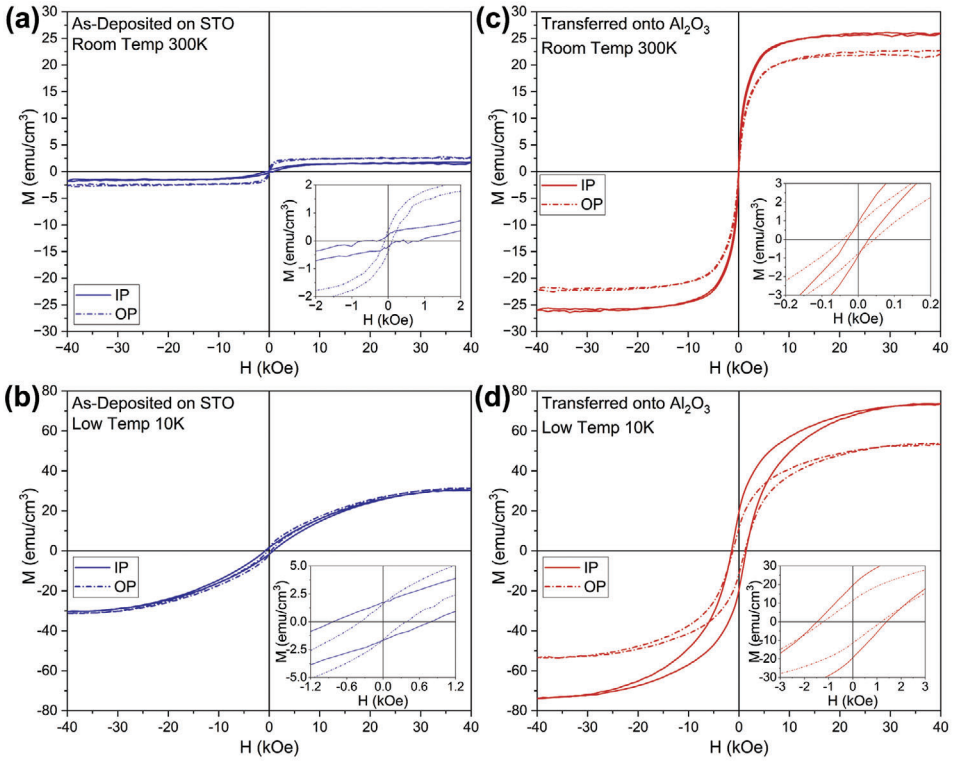

Figure 5. Magnetic property analysis of the BFMO films before and after transfer onto sapphire. M–H loops on the as-deposited on STO sample at a) room temperature and b) low temperature. M–H loops on the transferred sample at c) room temperature and d) low temperature. The measurement data is collected both when the magnetic field is applied in-plane (IP) and out-of-plane (OP) of the sample surface.

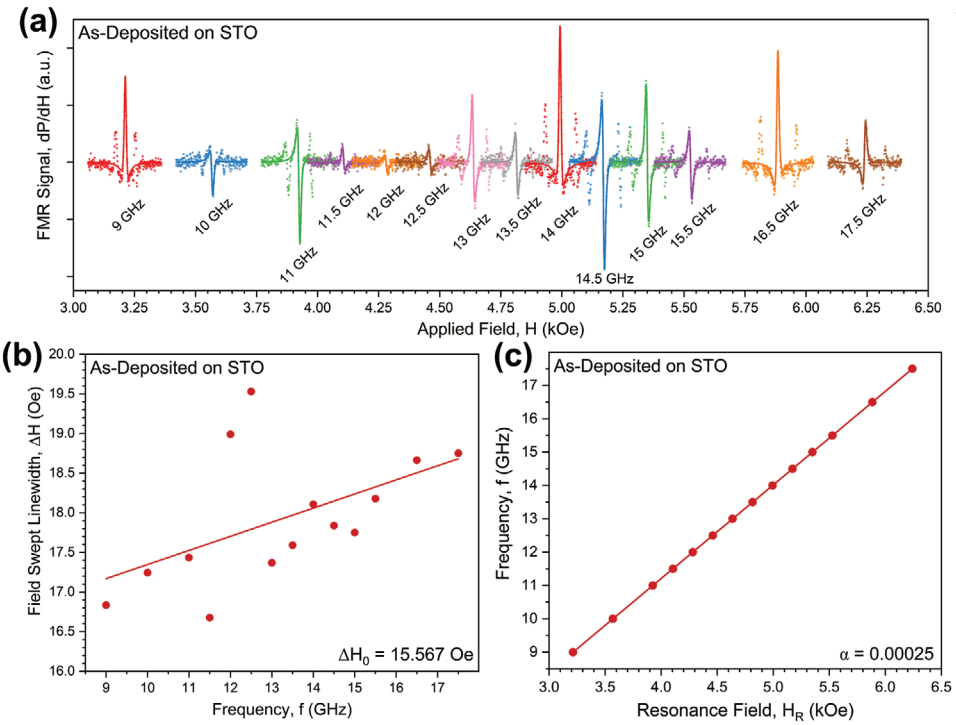

Figure 6. FMR analysis of as-deposited sample at 300 K. a) FMR signal data shown at each measurement frequency. b) Kittel plot of field-swept linewidth of the resonance peaks. c) Damping plot of resonance field at each measurement frequency.

cracks in the film caused by the partial strain relaxation observed in the XRD data. These microcracks could lead to division of the magnetic domains and elimination of the FMR effect. It is very interesting that we observed these promising FMR properties in the BFMO LSC films. Further work is needed to optimize the epoxy transfer process to minimize the microcrack formation and refine the FMR measurements for the transferred film.

These FMR results are promising for device applications, including acoustically driven ferromagnetic resonance (ADFMR), as the Gilbert damping coefficient is amazingly low. Materials such yttrium-iron-garnet (YIG) on gadolinium-gallium-garnet (GGG) are typically reported in the range of 10^{-5}–10^{-4}, only one order of magnitude lower than the BFMO LSC material reported here.[71–74] This type of high-Q resonance in FMR may be useful for applications such as FMR spectroscopy[75] and circulators for communication platforms.[76] The ability to transfer these BFMO films onto substrates such as silicon and lithium niobate using the method reported here opens the door to FMR-based devices.

3. Discussion

The rigid epoxy transfer method reported here has resulted in an unprecedented order-of-magnitude increase in the continuous area of transferred highly strained films (3 × 3 mm). This highly strained film cannot be readily transferred at this scale by existing methods, such as flexible polymer approaches. This new method enables transfer of films that were previously unachievable because of high strain or other factors. Surface analysis performed throughout the transfer process, including optical microscopy, SEM, and AFM, confirmed that the film surface remained in-tact, pristine, and crack-free over a large portion of the transferred area. Structure analysis was performed using XRD to show that the film was still nearly single crystal after transfer, with only a slight increase in the FWHM of the peaks. TEM confirmed high epitaxial quality, even with the epoxy layer securing the film to the new substrates. The magnetic properties before and after transfer were notably strong, with high saturation magnetization. Remarkably, the magnetic properties are enhanced after film transfer due to the release of the strain in the film. It is possible that substrate and epoxy control could further improve these results. Finally, the BFMO film is shown to possess strong FMR with exceedingly low damping and interesting triple peaks, possibly due to its unique periodic layered structure. These results are noteworthy as the Gilbert damping coefficient of the BFMO films are comparable to that of state-of-the-art FMR materials. The combination of successful, large-area thin film transfer and high-Q FMR enables potential ADFMR applications such as the ability to probe magnons[12] and fabrication of extremely sensitive magnetic field sensors.[54]

4. Experimental Section

Thin Film Growth: The $Bi_3Fe_2Mn_2O$ (BFMO), CeO_2, and $Sr_3Al_2O_6$ (SAO) oxide thin films studied in this work were deposited using pulsed laser deposition (PLD, Lambda Physik COMPex Pro 205 KrF ($\lambda = 248$ nm) Excimer Laser with Neocera Vacuum Chamber) on $SrTiO_3$ (STO) (001) substrates. A laser incidence angle of 45° and target-substrate distance of 4.5 cm were used. Prior to deposition, the STO substrates were cleaned using acetone, methanol, and isopropanol in a sonicator for 5 min each, rinsed with DI water for 60 s, and annealed at 1100 °C for 5 h in atmosphere. This generates atomically flat surfaces and primarily TiO_2 terminations.[77] Before deposition, the chamber was pumped to 10^{-6}–10^{-7} Torr. For the SAO layer, the deposition parameters included a laser energy of 420 mJ, substrate temperature of 830 °C, and atmosphere of 100 mT O_2. Since this layer was only used as a sacrificial layer, the thickness was not precisely measured but was estimated to be ≈100 nm. For the 45 nm CeO_2 layer, a laser energy of 450 mJ, substrate temperature of 750 °C, and atmosphere of 50 mT O_2 were used. Finally, a 150 nm BFMO film was deposited with a laser energy of 450 mJ, substrate temperature of 750 °C, and O_2 atmosphere of 200 mTorr. The samples were annealed post-deposition in 200 Torr O_2 while cooling at 10 °C min^{-1}. The BFMO target was made by sintering a pressed pellet of Bi_2O_3, MnO_2, and Fe_2O_3 powders for 3 h at 750 °C. The CeO_2 target was made by directly sintering a pressed pellet of CeO_2 powder for 10 h at 1200 °C.

Surface Characterization: Optical microscopy (Keyence VK-X150 3D Laser Scanning Confocal Microscope) of the entire film area was collected by stitching rastered images together, allowing for high resolution analysis across a large (5×10 mm) area. Atomic force microscopy (AFM, Bruker Dimension Icon) was collected using SCANASYST-AIR probes. The scanning electron microscopy (SEM, FEI NNL650) images were collected using a secondary electron detector.

Microstructure Characterization: X-ray diffractometry (XRD, PANalytical Empyrean) was done with a parallel beam configuration. Rocking curves were collected at the BFMO SC(004) peak due to its high relative intensity and distance from other peaks, allowing for unambiguous results. Transmission electron microscopy (TEM) and scanning TEM (STEM) was used to image the as-deposited on STO sample (Thermo-Fisher Themis Z) and the transferred sample (Thermo-Fisher TALOS F200X). The as-deposited sample was prepared for TEM using a manual hand-prep process with grinding, dimpling, and ion milling (Gatan PIPS 695). The transferred sample was prepared by lift-out via focused ion beam (FIB, Thermo Scientific Helios G4 UX Dual Beam). The two Pt layers observed in the images of the FIB sample were deposited by thermal evaporation, for providing conductivity during SEM imaging, and e-beam evaporation, for protecting the film during FIB milling.

Property Characterization: Magnetic M–H loop measurements were performed using a magnetic property measurement system (MPMS, Quantum Design MPMS-3 SQUID Magnetometer). The samples were measured at room temperature (300 K) and low temperature (10 K). The magnetization was measured in vibrating sample mode (VSM) as the applied magnetic field was swept to ±4 Tesla. The background diamagnetic signal was subtracted, resulting in the loop only showing the ferromagnetic contributions. The ferromagnetic resonance (FMR) measurements were performed using a physical property measurement system (PPMS, Quantum Design Dynacool), and a NanOsc Instruments CryoFMR system, and NanOsc PhaseFMR software. For each FMR microwave frequency (9–17.5 GHz) in the coplanar waveguide, the DC magnetic field was swept to collect the resonance/absorption peak.

Thin Film Transfer: The new sapphire and fused silica substrates were diced (Microautomation 1100 Dicing Saw) into 4×9 mm pieces. The films were originally deposited on 5 × 10 mm pieces of STO, so the new sapphire/fused silica substrates did not cover the entire film area. This was intentional so that the epoxy did not seal the SAO layer completely, which would have prevented the water from entering and dissolving it. The sapphire and fused silica substrates were cleaned with acetone, methanol, and isopropanol before bonding with epoxy. The as-deposited samples were cleaned only with methanol to prevent premature dissolution of the SAO. When the films were deposited, a CeO_2 buffer layer was added because of its well-known property of stabilizing the LSC phase of BFMO, which was desired.[17,19,20,22–24] The epoxy (Epo-Tek ET353ND Heat Cure Epoxy) was pressed between the original and new substrate to a thickness of ≈1 µm. The thickness of 1 µm was found to be repeatably obtained by pressing down as hard as possible with a tweezer at 75 °C for several minutes. The surface tension and viscosity of the epoxy at this temperature leads to this result. The light interference fringes generated by the thin layer of epoxy were used to ensure that the epoxy was of uniform thickness across the

sample length (i.e., the fringes were eliminated/minimized by pressing on different areas of the new, transparent substrate). These fringes can be seen in the bottom right corner of Figure 2b. The physics of light interference dictates that the absence of these fringes means the epoxy is of uniform epoxy thickness across the sample. The epoxy was then cured on a hot plate in steps at 75 °C for 40 min, 120 °C for 40 min, and, finally, 150 °C for 60 min, before cooling to room temperature on the hot plate to reduce thermally induced strain. The slow ramping of the temperature allows the epoxy to partially cure and lock the shape so that the relative thermal expansion difference between the materials involved does not cause excessive strain after cooling. The STO was then lapped (Allied Multiprep 12″ lapper) using diamond lapping paper (30, 15, 9, 6, and 3 µm) to a thickness of 30 µm. This lapping step was found to be necessary as it causes the remaining thin STO layer to pull away slightly from the film as the SAO dissolves due to residual strain, which allows the water to continue progressing through the gap. When the STO was not lapped before dissolution of the SAO, the water could not effectively progress along the SAO film to completely dissolve it as the diffusion through the small gap (≈100 nm) was not sufficient. A beaker of deionized (DI) water was used to dissolve the SAO sample. To increase the rate of dissolution, the water was heated to 75 °C and the beaker was placed into a sonicator. When heating and sonication were not used, the SAO would not entirely dissolve as the diffusivity of the water was not sufficient and the SAO could not be transported out of the area. The sample was left overnight to dissolve. When removed from the water, the sample was cleaned with new DI water, acetone, methanol, and isopropanol.

Supporting Information

Supporting Information is available from the Wiley Online Library or from the author.

Acknowledgements

The thin film growth effort was supported by the U.S. Office of Naval Research (N00014-20-1-2600). The film transfer effort was supported by the U.S. National Science Foundation (DMREF-2323753). Y.Z. and H.W. acknowledge the support from the U.S. National Science Foundation (DMR-2016453) for high resolution microscopy analysis. J.S. also acknowledges the support from the Purdue Bilsland Fellowship. I.B., J.N., H.J, O.M., and R.S. acknowledge the support from the U.S. Department of Energy, Office of Basic Energy Sciences, Division of Materials Sciences and Engineering (BES 20-017574). This work was performed, in part, at the Center for Integrated Nanotechnologies, an Office of Science User Facility operated for the U.S. Department of Energy (DOE) Office of Science. This article has been authored by an employee of the National Technology & Engineering Solutions of Sandia, LLC under Contract No. DE-NA0003525 with the U.S. Department of Energy (DOE). This work was performed under the Laboratory Directed Research and Development (LDRD) program at Sandia National Laboratories. Sandia National Laboratories is a multimission laboratory managed and operated by National Technology and Engineering Solutions of Sandia, LLC, a wholly owned subsidiary of Honeywell International Inc., for the U.S. Department of Energy's National Nuclear Security Administration under contract DE-NA0003525. This paper describes objective technical results and analysis. Any subjective views or opinions that might be expressed in the paper do not necessarily represent the views of the U.S. Department of Energy or the United States Government.

Conflict of Interest

The authors declare no conflict of interest.

Data Availability Statement

The data that support the findings of this study are available in the supplementary material of this article.

Keywords

bismuth oxides, ferromagnetic resonance, layered supercells, multiferroic thin films

Received: June 21, 2024
Revised: November 11, 2024
Published online: December 9, 2024

[1] D. I. Khomskii, *J. Magn. Magn. Mater.* **2006**, *306*, 1.
[2] S.-W. Cheong, M. Mostovoy, *Nat. Mater.* **2007**, *6*, 13.
[3] J. P. Velev, C.-G. Duan, J. D. Burton, A. Smogunov, M. K. Niranjan, E. Tosatti, S. S. Jaswal, E. Y. Tsymbal, *Nano Lett.* **2009**, *9*, 427.
[4] T. Kosub, M. Kopte, R. Hühne, P. Appel, B. Shields, P. Maletinsky, R. Hübner, M. O. Liedke, J. Fassbender, O. G. Schmidt, D. Makarov, *Nat. Commun.* **2017**, *8*, 13985.
[5] M. Bibes, A. Barthélémy, *Nat. Mater.* **2008**, *7*, 425.
[6] C. Chen, D. Chen, P. Li, M. Qin, X. Lu, G. Zhou, X. Gao, J. Liu, *Adv. Funct. Mater.* **2023**, *33*, 2208244.
[7] J. F. Scott, *Nat. Mater.* **2007**, *6*, 256.
[8] F. Yang, M. H. Tang, Z. Ye, Y. C. Zhou, X. J. Zheng, J. X. Tang, J. J. Zhang, J. He, *J. Appl. Phys.* **2007**, *102*, 044504.
[9] D. A. Bas, P. J. Shah, A. Matyushov, M. Popov, V. Schell, R. C. Budhani, G. Srinivasan, E. Quandt, N. Sun, M. R. Page, *IEEE Trans. Magn.* **2021**, *57*, 1.
[10] P. J. Shah, D. A. Bas, I. Lisenkov, A. Matyushov, N. X. Sun, M. R. Page, *Sci. Adv.* **2020**, *6*, eabc5648.
[11] D. Labanowski, A. Jung, S. Salahuddin, *Appl. Phys. Lett.* **2016**, *108*, 022905.
[12] D. A. Bas, P. J. Shah, M. E. McConney, M. R. Page, *J. Appl. Phys.* **2019**, *126*, 114501.
[13] C. F. Doiron, I. Brener, A. Cerjan, in *Conf. on Lasers and Electro-Optics*, Optica Publishing Group, MA **2022**.
[14] S. D. Gennaro, C. F. Doiron, N. Karl, P. P. Iyer, D. K. Serkland, M. B. Sinclair, I. Brener, *ACS Photonics* **2022**, *9*, 1026.
[15] A. Desmet, A. Radosavljevic, J. Missinne, D. Van Thourhout, G. Van Steenberge, *IEEE Photonics J.* **2021**, *13*, 2400112.
[16] Y. Zhu, A. Chen, H. Zhou, W. Zhang, J. Narayan, J. L. MacManus-Driscoll, Q. Jia, H. Wang, *APL Mater.* **2013**, *1*, 050702.
[17] L. Li, W. Zhang, F. Khatkhatay, J. Jian, M. Fan, Q. Su, Y. Zhu, A. Chen, P. Lu, X. Zhang, H. Wang, *ACS Appl. Mater. Interfaces* **2015**, *7*, 11631.
[18] W. Zhang, M. Li, A. Chen, L. Li, Y. Zhu, Z. Xia, P. Lu, P. Boullay, L. Wu, Y. Zhu, J. L. MacManus-Driscoll, Q. Jia, H. Zhou, J. Narayan, X. Zhang, H. Wang, *ACS Appl. Mater. Interfaces* **2016**, *8*, 16845.
[19] A. Chen, H. Zhou, Y. Zhu, L. Li, W. Zhang, J. Narayan, H. Wang, Q. Jia, *J. Mater. Res.* **2016**, *31*, 3530.
[20] L. Li, J. Cheng, H. Wang, J. Huang, X. Gao, X. Wang, S. Misra, B. Zhang, J. Jian, A. Chen, P. Lu, X. Qian, K. Yang, H. Wang, *Cryst. Growth Des.* **2019**, *19*, 7088.
[21] Z. He, X. Gao, D. Zhang, P. Lu, X. Wang, M. Kalaswad, B. X. Rutherford, H. Wang, *NanoscaleNanoscale* **2021**, *13*, 16672.
[22] J. P. Barnard, J. Shen, Y. Zhang, J. Lu, J. Song, A. Siddiqui, R. Sarma, H. Wang, *Nanoscale Adv.* **2023**, *5*, 5850.
[23] J. P. Barnard, R. L. Paldi, M. Kalaswad, Z. He, H. Dou, Y. Zhang, J. Shen, D. Zheng, N. R. Dilley, R. Sarma, A. M. Siddiqui, P. D. Ye, H. Wang, *Cryst. Growth Des.* **2023**, *23*, 2248.
[24] A. Chen, H. Zhou, Z. Bi, Y. Zhu, Z. Luo, A. Bayraktaroglu, J. Phillips, E. Choi, J. L. MacManus-Driscoll, S. J. Pennycook, J. Narayan, Q. Jia, X. Zhang, H. Wang, *Adv. Mater.* **2013**, *25*, 1028.
[25] J. Huang, J. L. MacManus-Driscoll, H. Wang, *J. Mater. Res.* **2017**, *32*, 4054.
[26] J. Shen, J. P. Barnard, H. Wang, *APL Mater.* **2024**, *12*, 040601.

[27] J. P. Barnard, J. Shen, B. K. Tsai, Y. Zhang, M. R. Chhabra, K. Xu, X. Zhang, R. Sarma, A. Siddiqui, H. Wang, *Small Sci.* **2024**, *4*, 2400114.
[28] P. Khan, M. Kanamaru, K. Matsumoto, T. Ito, T. Satoh, *Phys. Rev. B* **2020**, *101*, 134413.
[29] D. Talbayev, S. Lee, S.-W. Cheong, A. J. Taylor, *Appl. Phys. Lett.* **2008**, *93*, 212906.
[30] B. Peng, Q. Lu, H. Tang, Y. Zhang, Y. Cheng, R. Qiu, Y. Guo, Z. Zhou, M. Liu, *Mater. Horiz.* **2022**, *9*, 3013.
[31] K. P. Pandey, *FerroelectricsFerroelectrics* **2020**, *558*, 140.
[32] M. Kalaswad, B. Zhang, X. Wang, H. Wang, X. Gao, H. Wang, *Nanoscale Adv.* **2020**, *2*, 4172.
[33] M. Hamrouni, M. Jankowski, A. Y. Hwang, N. Flemens, J. Mishra, C. Langrock, A. H. Safavi-Naeini, M. M. Fejer, T. Südmeyer, *Opt. Express* **2024**, *32*, 12004.
[34] W. E. Angerer, N. Yang, A. G. Yodh, M. A. Khan, C. J. Sun, *Phys. Rev. B* **1999**, *59*, 2932.
[35] M. Kalaswad, B. Zhang, H. Wang, X. Wang, J. Huang, H. Wang, *Mater. Today Adv.* **2020**, *8*, 100112.
[36] M. Kalaswad, D. Zhang, X. Gao, L. L. Contreras, H. Wang, X. Wang, H. Wang, *ACS Appl. Mater. Interfaces* **2019**, *11*, 45199.
[37] J. Shen, B. K. Tsai, K. Xu, A. Shang, J. P. Barnard, Y. Zhang, R. Tripathi, Z. Chen, X. Zhang, H. Wang, *Nano Res.* **2023**, *16*, 10559.
[38] C. M. Went, J. Wong, P. R. Jahelka, M. Kelzenberg, S. Biswas, M. S. Hunt, A. Carbone, H. A. Atwater, *Sci. Adv.* **2019**, *5*, eaax6061.
[39] D. Pesquera, E. Parsonnet, A. Qualls, R. Xu, A. J. Gubser, J. Kim, Y. Jiang, G. Velarde, Y. Huang, H. Y. Hwang, R. Ramesh, L. W. Martin, *Adv. Mater.* **2020**, *32*, 2003780.
[40] D. G. Purdie, N. M. Pugno, T. Taniguchi, K. Watanabe, A. C. Ferrari, A. Lombardo, *Nat. Commun.* **2018**, *9*, 5387.
[41] D. Lu, D. J. Baek, S. S. Hong, L. F. Kourkoutis, Y. Hikita, H. Y. Hwang, *Nat. Mater.* **2016**, *15*, 1255.
[42] F. Pizzocchero, L. Gammelgaard, B. S. Jessen, J. M. Caridad, L. Wang, J. Hone, P. Bøggild, T. J. Booth, *Nat. Commun.* **2016**, *7*, 11894.
[43] T. Zhang, G. Yao, T. Pan, Q. Lu, Y. Lin, *J. Semicond.* **2020**, *41*, 041602.
[44] G. Dong, S. Li, M. Yao, Z. Zhou, Y.-Q. Zhang, X. Han, Z. Luo, J. Yao, B. Peng, Z. Hu, H. Huang, T. Jia, J. Li, W. Ren, Z.-G. Ye, X. Ding, J. Sun, C.-W. Nan, L.-Q. Chen, J. Li, M. Liu, *ScienceScience* **2019**, *366*, 475.
[45] L. Wang, I. Meric, P. Y. Huang, Q. Gao, Y. Gao, H. Tran, T. Taniguchi, K. Watanabe, L. M. Campos, D. A. Muller, J. Guo, P. Kim, J. Hone, K. L. Shepard, C. R. Dean, *ScienceScience* **2013**, *342*, 614.
[46] D. Lu, S. Crossley, R. Xu, Y. Hikita, H. Y. Hwang, *Nano Lett.* **2019**, *19*, 3999.
[47] P. Salles, I. Caño, R. Guzman, C. Dore, A. Mihi, W. Zhou, M. Coll, *Adv. Mater. Interfaces* **2021**, *8*, 2001643.
[48] Z. Zhao, A. Abdelsamie, R. Guo, S. Shi, J. Zhao, W. Lin, K. Sun, J. Wang, J. Wang, X. Yan, J. Chen, *Nano Res.* **2022**, *15*, 2682.
[49] F. An, K. Qu, G. Zhong, Y. Dong, W. Ming, M. Zi, Z. Liu, Y. Wang, B. Qi, Z. Ding, J. Xu, Z. Luo, X. Gao, S. Xie, P. Gao, J. Li, *Adv. Funct. Mater.* **2020**, *30*, 2003495.
[50] B. Peng, R.-C. Peng, Y.-Q. Zhang, G. Dong, Z. Zhou, Y. Zhou, T. Li, Z. Liu, Z. Luo, S. Wang, Y. Xia, R. Qiu, X. Cheng, F. Xue, Z. Hu, W. Ren, Z.-G. Ye, L.-Q. Chen, Z. Shan, T. Min, M. Liu, *Sci. Adv.* **2020**, *6*, eaba5847.
[51] G. Dong, Y. Hu, C. Guo, H. Wu, H. Liu, R. Peng, D. Xian, Q. Mao, Y. Dong, Y. Zhao, B. Peng, Z. Wang, Z. Hu, J. Zhang, X. Wang, J. Hong, Z. Luo, W. Ren, Z. Ye, Z. Jiang, Z. Zhou, H. Huang, Y. Peng, M. Liu, *Adv. Mater.* **2022**, *34*, 2108419.
[52] Y. Kim, S. S. Cruz, K. Lee, B. O. Alawode, C. Choi, Y. Song, J. M. Johnson, C. Heidelberger, W. Kong, S. Choi, K. Qiao, I. Almansouri, E. A. Fitzgerald, J. Kong, A. M. Kolpak, J. Hwang, J. Kim, *NatureNature* **2017**, *544*, 340.
[53] A. Jain, P. Bharadwaj, S. Heeg, M. Parzefall, T. Taniguchi, K. Watanabe, L. Novotny, *NanotechnologyNanotechnology* **2018**, *29*, 265203.
[54] S. Salahuddin, D. E. Labanowski, *Magnetic Field Sensor Using Acoustically Driven Ferromagnetic Resonance*, **2023**.
[55] Q. Li, C. X. Trang, W. Wu, J. Hwang, D. Cortie, N. Medhekar, S. Mo, S. A. Yang, M. T. Edmonds, *Adv. Mater.* **2022**, *34*, 2107520.
[56] H. Wang, Y. Liu, P. Wu, W. Hou, Y. Jiang, X. Li, C. Pandey, D. Chen, Q. Yang, H. Wang, D. Wei, N. Lei, W. Kang, L. Wen, T. Nie, W. Zhao, K. L. Wang, *ACS Nano* **2020**, *14*, 10045.
[57] J. Zhang, T. Lin, A. Wang, X. Wang, Q. He, H. Ye, J. Lu, Q. Wang, Z. Liang, F. Jin, S. Chen, M. Fan, E.-J. Guo, Q. Zhang, L. Gu, Z. Luo, L. Si, W. Wu, L. Wang, *ScienceScience* **2024**, *383*, 388.
[58] B. Zhang, C. Yun, J. L. MacManus-Driscoll, *Nanomicro Lett.* **2021**, *13*, 39.
[59] Y. Li, E. Zatterin, M. Conroy, A. Pylypets, F. Borodavka, A. Björling, D. J. Groenendijk, E. Lesne, A. J. Clancy, M. Hadjimichael, D. Kepaptsoglou, Q. M. Ramasse, A. D. Caviglia, J. Hlinka, U. Bangert, S. J. Leake, P. Zubko, *Adv. Mater.* **2022**, *34*, 2106826.
[60] S. S. Hong, J. H. Yu, D. Lu, A. F. Marshall, Y. Hikita, Y. Cui, H. Y. Hwang, *Sci. Adv.* **2017**, *3*, eaao5173.
[61] S. Gritschneder, Y. Namai, Y. Iwasawa, M. Reichling, *Nanotechnology Nanotechnology* **2005**, *16*, S41.
[62] S. Torbrügge, M. Cranney, M. Reichling, *Appl. Phys. Lett.* **2008**, *93*, 073112.
[63] R. L. Paldi, X. Sun, X. L. Phuah, J. Lu, X. Zhang, A. Siddiqui, H. Wang, *Nanoscale Adv.* **2021**, *3*, 2870.
[64] A. T. Raghavender, N. H. Hong, C. Park, M.-H. Jung, K. J. Lee, D. Lee, *Mater. Lett.* **2011**, *65*, 2786.
[65] A. Agbelele, D. Sando, I. C. Infante, C. Carrétéro, S. Jouen, J.-M. Le Breton, A. Barthélémy, B. Dkhil, M. Bibes, J. Juraszek, *Appl. Phys. Lett.* **2016**, *109*, 042902.
[66] Q. Gan, R. A. Rao, C. B. Eom, J. L. Garrett, M. Lee, *Appl. Phys. Lett.* **1998**, *72*, 978.
[67] K. Gas, M. Sawicki, *MaterialsMaterials* **2022**, *15*, 8532.
[68] Epo-Tek ET353ND Heat Cure Epoxy, https://focenter.com/epo-tekr-et353nd-heat-cure-epoxy-4g-1170 (accessed: May 2024).
[69] E. Coy, I. Fina, K. Załęski, A. Krysztofik, L. Yate, L. Rodriguez, P. Graczyk, H. Głowiński, C. Ferrater, J. Dubowik, M. Varela, *Phys. Rev. Appl.* **2018**, *10*, 054072.
[70] B. Luk'yanchuk, N. I. Zheludev, S. A. Maier, N. J. Halas, P. Nordlander, H. Giessen, C. T. Chong, *Nat. Mater.* **2010**, *9*, 707.
[71] K. Yamada, K. Kogiso, Y. Shiota, M. Yamamoto, A. Yamaguchi, T. Moriyama, T. Ono, M. Shima, *J. Magn. Magn. Mater.* **2020**, *513*, 167253.
[72] Q. B. Liu, K. K. Meng, Z. D. Xu, T. Zhu, X. G. Xu, J. Miao, Y. Jiang, *Phys. Rev. B* **2020**, *101*, 174431.
[73] R. Torrão, O. C. Alves, B. S. Archanjo, L. C. Sampaio, F. Garcia, *J. Alloys Compd.* **2022**, *923*, 166300.
[74] P. Trempler, R. Dreyer, P. Geyer, C. Hauser, G. Woltersdorf, G. Schmidt, *Appl. Phys. Lett.* **2020**, *117*, 232401.
[75] P. Bertrand, *Electron Paramagnetic Resonance Spectroscopy*, Springer International Publishing, Cham, **2020**.
[76] V. G. Harris, A. S. Sokolov, *J. Supercond. Nov. Magn.* **2019**, *32*, 97.
[77] F. Gellé, R. Chirita, D. Mertz, M. V. Rastei, A. Dinia, S. Colis, *Surf. Sci.* **2018**, *677*, 39.